

Temperature Dependence of Carbon Nanotube Growths

Joshua Alden

Biomedical Engineering, Georgia Institute of Technology

NNIN REU Site: Cornell NanoScale Science and Technology Facility, Cornell University, Ithaca, NY

NNIN REU Principal Investigator: Paul McEuen, Department of Physics, Laboratory of Atomic and Solid State Physics and Kavli Institute for Nanoscale Science, Cornell University

NNIN REU Mentor: Alejandro Cortese, Department of Physics, Cornell University

Contact: joshualden@gmail.com, pmceuen@gmail.com, ajc383@cornell.edu

Introduction:

Carbon nanotubes (CNTs) have unique electrical and physical properties that make them candidates for many different applications ranging from high-speed field-effect transistors to biosensors. For reliability and efficiency in such applications, it is important to run many devices in parallel, which requires nanotubes to be grown in consistent arrays at appropriate densities. In this project we explored how nanotube growth temperature is correlated with carbon nanotube density, nanotube diameter, and catalyst size. We also investigated the accuracy with which an atomic force microscope (AFM) measures nanotube diameter. Being nature's smallest wire, nanotubes have the potential to act as biosensors capable of sensing small molecules such as individual nucleotides in DNA. The sensitivity of these biosensors would then be dependent on the nanotube diameter, thus making it an important point of study.

Experimental Procedure:

Carbon nanotubes are grown from iron catalyst nanoparticles on quartz wafers in a high temperature chemical vapor deposition process, as illustrated in Figure 1. The quartz wafers used are ST cut, which means that they have atomic-scale terraces running in parallel across the wafer. Nanotubes can grow along these, leading to arrays of aligned nanotubes. Wafers were fabricated and nanotubes grown using standard procedures [1,2].

Following growth, AFM imaging was used to collect the heights and thus the diameters of the iron catalyst particles after growth and the diameters of the nanotubes while SEM imaging was used to measure the density of nanotubes after each growth. To calibrate the AFM nanotube diameter measurements, AFM-measured nanotubes from a quartz substrate were transferred onto TEM grids. The nanotubes were then imaged again using transmission electron microscopy (TEM) and their diameters were measured.

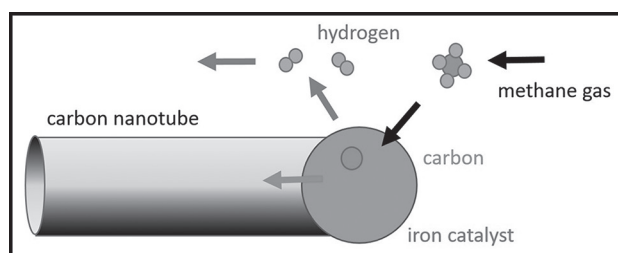


Figure 1: Chemical vapor deposition. Methane gas flows near an iron catalyst which absorbs the carbon into itself, and after saturation, the carbon moves to the outside of the catalyst and begins to form a nanotube.

Results and Discussion:

In the temperature range from 855°C to 915°C, we observed that average catalyst diameter increases with increasing temperature as shown in Figure 2a. However, the width of the distribution of catalyst sizes within each growth was larger than the observed increase. Ostwald ripening is the phenomenon suspected to be causing this trend. As temperature goes up, the iron atoms gain the energy necessary to migrate from smaller catalyst particles to larger ones, since this minimizes the number of atoms exposed at the surface. As a result, larger catalysts form during higher temperature growths.

We also observed a strong temperature-dependence to number of nanotubes per micron that grew from a given catalyst line, as shown in Figure 3. We noticed that CNTs grown at 855°C have low number density as can be seen in Figure 3a. Between 870°C and 885°C, the nanotubes grow at high densities, as in Figure 3b. Above 885°C, the density tapers off to 0, as seen in the

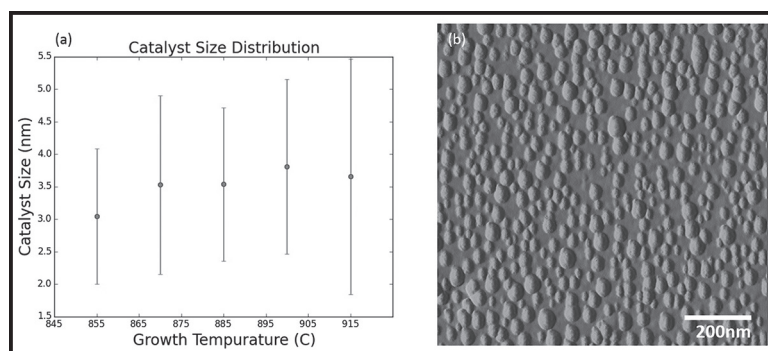


Figure 2: a) Catalyst size increased with increasing temperature. The dots and lines show respectively, the mean and standard deviation of observed catalyst sizes by AFM. b) AFM image of catalysts after an 870°C growth.

image in Figure 3c. Because nanotubes grow from the surface of catalyst particles, catalyst size and nanotube density are linked together. Once the catalysts reach an optimal size, many nanotubes will grow thus creating a high density of CNTs at that temperature. But at higher temperature growths, many of the catalysts are too large to initiate growth as resulting in a lower density as observed in Figure 3d.

Figure 4a shows AFM measurements of the average nanotube diameter as a function of temperature. The average nanotube diameter increases with increasing temperature. To calibrate these measurements, which can have systematic error due to tip-substrate interactions, one of the samples was AFM'd, then TEM'd. The resulting histogram of observed diameters is shown in Figure 4b. The more-accurate TEM measurements measured larger nanotube diameters than the AFM (Figure 4b).

In summary, we found that catalyst size, and nanotube diameter increase with increasing temperature and that nanotube density is tightly linked with the catalyst size. Knowing the temperature-dependence of carbon nanotubes on temperature allows us to reliably grow nanotubes of a pre-selected density and diameter, bringing wafer-scale production of nanotube biosensor arrays one step closer to viability.

Future Work:

Having developed an understanding and methodology for nanotube growth in a 5-inch furnace, we can now begin testing 4-inch wafer growths. If our methods successfully scale, this work will be used in the McEuen group's work on developing arrays of DNA sequencing devices. Other interesting expansions of this project include varying parameters such as the anneal time, and hydrogen and methane flow times and rates to create more uniform catalyst sizes with a narrower distribution. This may allow for more precise control over nanotube diameter and possibly a more exact density-temperature relationship.

Acknowledgments:

I would like to thank my mentor Alejandro Cortese and fellow lab members Jonathan Alden and Bryce Kobrin for their help and support on this project. I would also like to thank the McEuen lab and CNF for a positive and productive work environment. This research was supported

by the National Nanotechnology Infrastructure Network Research Experience for Undergraduates (NNIN REU) Program and National Science Foundation under Grant No. ECCS-0335765.

References:

- [1] Ding, L.; Yuan, D.; Liu, J. "Growth of High-Density Parallel Arrays of Long Single-Walled Carbon Nanotubes on Quartz Substrates." *J. Am. Chem. Soc.* 130, 5428-5429, 2008.
- [2] Kocabas, C.; Hur, S.-H.; Gaur, A.; Meitl, M. A.; Shim, M.; Rogers, J. A. "Guided Growth of Large-Scale, Horizontally Aligned Arrays of Single-Walled Carbon Nanotubes and Their Use in Thin Film Transistors." *Small* 1, 1110-1116, 2005.

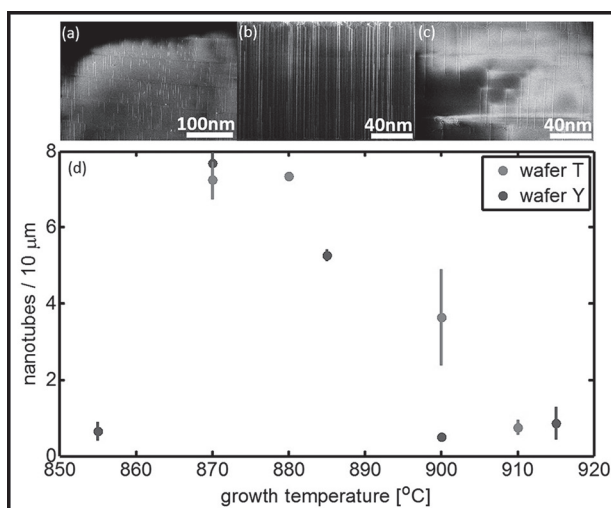


Figure 3: a) SEM image of nanotubes after an 855°C growth. b) SEM image of nanotubes after an 885°C growth. c) SEM image of nanotubes after a 915°C growth. d) Nanotube Density vs. Temperature. The dots and lines show respectively, the mean and standard deviation of the measured nanotube densities. The two different wafers are from two different fabrication batches and growths.

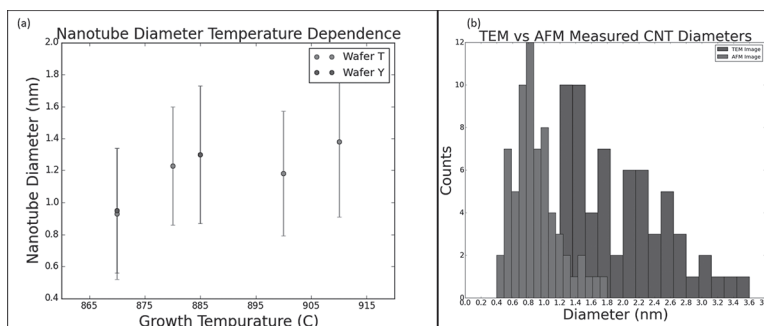


Figure 4: a) Shows the mean and standard deviation of AFM measured nanotubes from two separately fabricated wafers. b) Shows a histogram of the nanotube diameters measured by the AFM and TEM.

Determining the Spin Hall Angle of Gadolinium

Robyn Collette

Physics and Mathematics, Shippensburg University

NNIN REU Site: Cornell NanoScale Science and Technology Facility, Cornell University, Ithaca, NY

NNIN REU Principal Investigator: Dan Ralph, Physics Department, Cornell University

NNIN REU Mentor: Jonathan Gibbons, Physics Department, Cornell University

Contact: rcollette12@gmail.com, dcr14@cornell.edu, jg833@cornell.edu

Abstract:

The spin Hall effect is observed when electrons from a charge current are deflected based on their spin orientation, causing an accumulation of spins on the boundaries of a material. The spins can then exert a torque on an adjacent ferromagnetic material, potentially manipulating the orientation of the magnetization. It has been found that manipulating nanomagnets through spin transfer torques is much more practical than using a magnetic field. Therefore, spin transfer torques present advantages in non-volatile magnetic memory applications [1]. Spin-torque ferromagnetic resonance (STFMR) measurements were performed on various gadolinium-ferromagnetic multilayers, and the spin Hall angle was extracted. The anisotropic magnetoresistance (AMR) of Py and CoFeB was measured. The saturation magnetization, the conductivity of Gd, and the x-factor were also measured for use in analysis. It was found that the spin Hall angle of Gd is 2%.

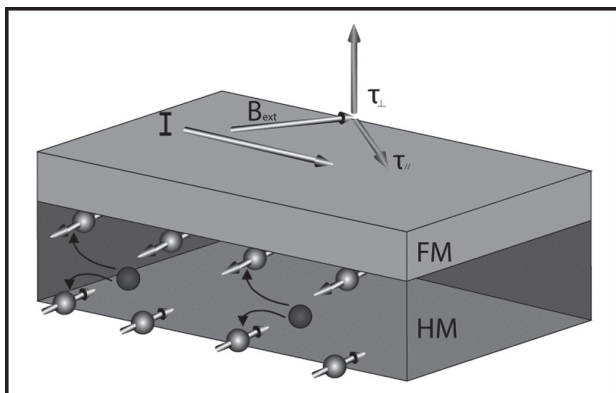


Figure 1: Stack device of a heavy metal (HM) and a ferromagnetic material (FM). Electrons deflected based on their spin orientation. Torque exerted on adjacent layer magnetization can be observed.

electrons from a charge current are deflected based on their spin orientation, causing an accumulation of spins on the boundaries of a material. The spins can then exert a torque on an adjacent ferromagnetic material, potentially manipulating the orientation of the magnetization as seen in Figure 1. The effectiveness of the spin Hall effect in a given material is described by the spin Hall angle, a ratio of the generated spin current to the applied charge current.

Experimental Procedure:

Material stacks of 10 nm of gadolinium (Gd) and 5 to 10 nm of a ferromagnetic material were deposited on a sapphire wafer through sputter deposition. Permalloy (a NiFe alloy) or cobalt iron boron (CoFeB) were used as the ferromagnetic layer. Hall bars were then patterned through

Introduction:

Technology is rapidly evolving, presenting a need for a universal memory that is nonvolatile, has a high storage density, and has a fast access time. One solution for this is magnetoresistive random access memory (MRAM). In MRAM, information is stored in the magnetization state of a nanomagnet; this information is read and written electronically. Research has successfully developed a way to easily read the state, but manipulating the state effectively still poses a problem. One method of manipulating the magnetization state being explored in current research is spin transfer torques. Spin transfer torques are caused by the spin Hall effect. The spin Hall effect is observed when

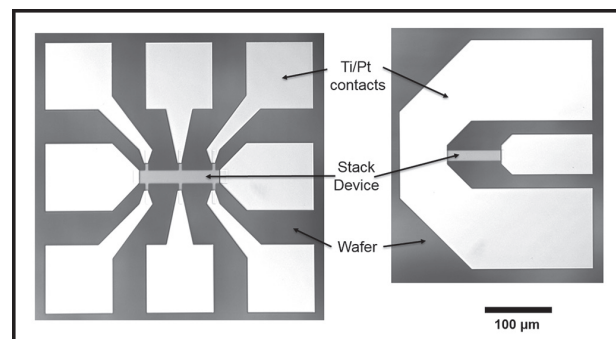


Figure 2: (Left) Device geometry used for STFMR measurements. (Right) Device geometry used for resistance measurements. The Hall bars shown are 80 μm by 24 μm .

optical photolithography and ion milling procedures. Platinum contacts were deposited through sputter deposition. Various device geometries were fabricated to accommodate electrical measurement set ups, as seen in Figure 2.

Devices were characterized using spin-torque ferromagnetic resonance (STFMR) measurements. An RF ground-signal-ground probe was connected to the device. A fixed microwave frequency was applied to the sample while sweeping an in-plane magnetic field from -0.25 T to 0.25 T. The magnetization of the ferromagnet precessed due to the oscillating current induced torque, which yielded an oscillating anisotropic magnetoresistance (AMR). The AMR and applied ac current were used to calculate the mixing voltage. This mixing voltage was recorded against the magnetic fields over a range of applied frequencies [2].

AMR is observed when the resistance of a material has a dependence on the angle between the current direction and the magnetization direction. Since this angle changes during STFMR measurements, the AMR of each sample was characterized in order to properly analyze the spin Hall angle.

The saturation magnetization, conductivity of gadolinium and x-factor (a ratio of stack resistance to the resistance of gadolinium) were measured for use in the analysis.

Results and Conclusions:

This analysis was run on four different sample stacks. The results of the analysis are compiled in Figure 3. It was determined that the spin Hall angle of gadolinium is about 2%. There is a sign ambiguity that would require further analysis to determine whether the spin Hall angle is positive or negative. Based on the resistance measurements of the sample stacks, there likely is a problem with Py grown on Gd. However, a 2 nm Hf spacer seems to alleviate this in the Gd/Py samples; this problem is not seen in the Gd/CoFeB samples.

Future Work:

More analysis will be done on other devices to ensure the accuracy of the spin Hall angle. The sign of the spin Hall angle will also be further explored. The difficulty of growing Py on Gd will also be examined to determine why the problem occurs.

Acknowledgments:

I would like to thank my principal investigator, Dan Ralph, as well as my mentor, Jonathan Gibbons. I would like to thank Neal Reynolds and the rest of the Ralph group members. I would like to thank the CNF REU Program Coordinators, Melanie-Claire Mallison, Lynn Rathbun, and Michael Skvarla as well as the CNF staff. I would also like to thank the National Science Foundation, the National Nanotechnology Infrastructure Network, and the Cornell NanoScale Science & Technology Facility for funding (under Grant No. ECCS-0335765) and facility use.

References:

- [1] Liu, L., Moriyama, T., Ralph, D. C., and Buhrman, R. A. Spin-Torque Ferromagnetic Resonance Induced by the Spin Hall Effect. *Phys. Rev. Lett.* 106, 036601 (2011).
- [2] Mellnik, A. R. (2015). Measurements of spin torques generated by topological insulators and heavy metals. (Doctoral Dissertation). Cornell University, Ithaca, NY.

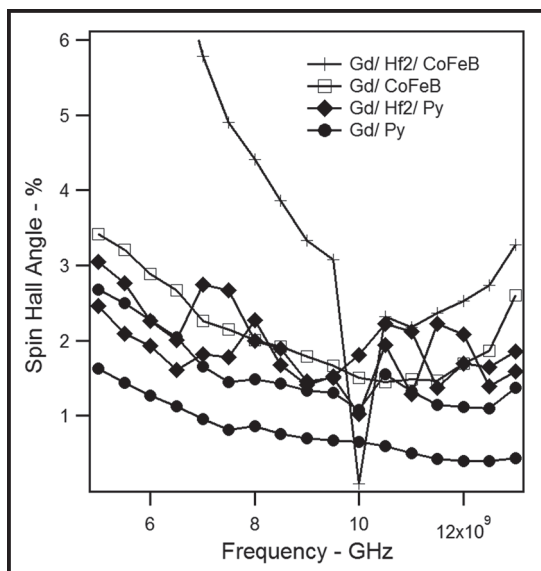


Figure 3: Compiled results of spin Hall angle analysis for six different devices. Spin Hall angle axis is cut off at 5% in order to better see what is recorded around 2%.

Design and Fabrication of Plasmonic Device for MIR Absorption Spectroscopy

Jacob Heppner

Applied Physics and Computer Science, Bethel University

NNIN REU Site: Minnesota Nano Center, University of Minnesota-Twin Cities, Minneapolis, MN

NNIN REU Principal Investigator: Prof. Sang-Hyun Oh, Electrical and Computer Engineering, University of Minnesota

NNIN REU Mentors: Daniel Mohr, Daniel Klemme*, and Daehan Yoo; Electrical and Computer Engineering, University of Minnesota

(* 2012 NNIN REU Intern at University of Colorado)

Contact: jah73854@bethel.edu, sang@umn.edu, mohrx117@umn.edu, klemm023@umn.edu, yooxx094@umn.edu

Abstract:

Plasmonic structures, such as slits, grooves, or apertures in metal films can be used to guide optical energy beyond the conventional diffraction limit of light, allowing for optical measurements that would not be possible with standard techniques. Annular nanoapertures have been utilized for applications in plasmonic sensing and spectroscopy. We have developed a fabrication technique to utilize strongly enhanced plasmonic fields in such structures. These techniques allow small changes in the absorption or reflection spectra of the device to detect compounds within close proximity to the structures. It is expected that device sensitivity will be increased through the reduction of critical dimensions.

Introduction:

Surface plasmon polaritons (SPPs) are hybrid electromagnetic waves across a metallic interface that are commonly excited by coupling light to conduction electron plasma. The electromagnetic field from SPPs can be confined to a smaller volume with much greater intensity than is possible using conventional diffractive optics. These properties make plasmonically-active patterned metal films ideal candidates for a variety of optical sensing applications. In particular, plasmonic biosensors have been used for observing association and dissociation in binding kinetics, lowering the limit of detection of analyte in solution, and detection of known particles in solution using spectroscopy. These biosensors are metallic nanostructures that have been engineered to increase confinement of plasmons and create regions of high field enhancement.

In this work, we present the design and fabrication of annular nanogaps tuned to operate plasmonically in the mid-infrared (MIR) region of the electromagnetic spectrum. An annular nanogap is a coaxial structure where an annular gap is formed in a conducting material that is attached to the substrate. These annular nanogaps were created using a lift-off process.

Experimental Procedure:

The first step of the process was spin coating flowable oxide-16 photoresist (FOx-16), a negative tone resist, on a calcium fluoride substrate. A 5 nm thick layer of gold was then sputtered on the insulating substrate to prevent unwanted charging during the exposure. The FOx-16 was

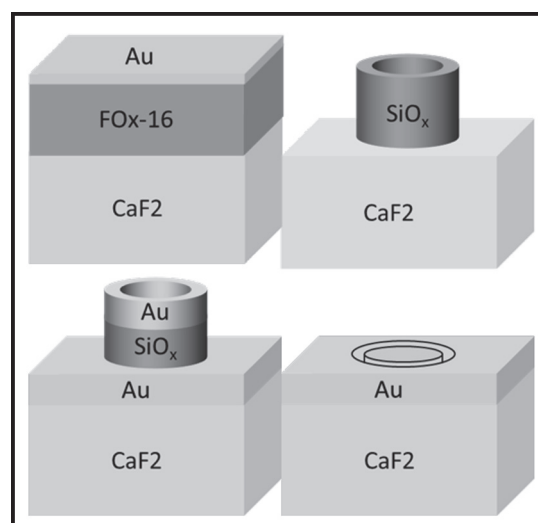


Figure 1: Process diagram for annular nanogap fabrication.

then exposed using electron-beam (e-beam) lithography, after which the sample was developed in a 1% NaOH 4% NaCl solution. Gold, 100 nm thick, was then evaporated onto the sample by electron-beam evaporation. The sample was then sonicated in buffered oxide etch to dissolve the photoresist in the annular gaps, lifting the gold above this region. This process is shown in Figure 1. FOx-16 was chosen because it is a negative tone resist that can be spun on at large thicknesses and it would not react with the potassium iodide that we used to etch the gold discharge layer before developing.

We would like to use these annular nanogaps for MIR absorption spectroscopy to identify molecular species. These annular nanogaps will focus light into regions of high field enhancement, which will provide high sensitivity to identifying particular molecular species. One of the advantages of using an annular nanogap structure above using a thin film of gold is the ability to tune the structure to the MIR region of the electromagnetic spectrum, which is important for vibrational absorption spectroscopy of molecules. The critical dimensions on device performance are the gap width, inner radius of the annular gap, and the thickness of the metal film. The thickness was chosen to be 100 nm to balance plasmonic enhancement of the sensor and the transmission through the sensor, maximizing the signal to noise of the device. Both 300 nm and 700 nm inner radius annular gaps were fabricated, each having the same 200 nm gap width to test to different regions within the MIR.

Full fabrication of the annular nanogaps was accomplished on a silicon substrate (Figures 2 and 3). These samples were characterized using Fourier transform infrared spectroscopy, and simulations of the structures using the finite-difference time-domain technique were also performed (Figure 4).

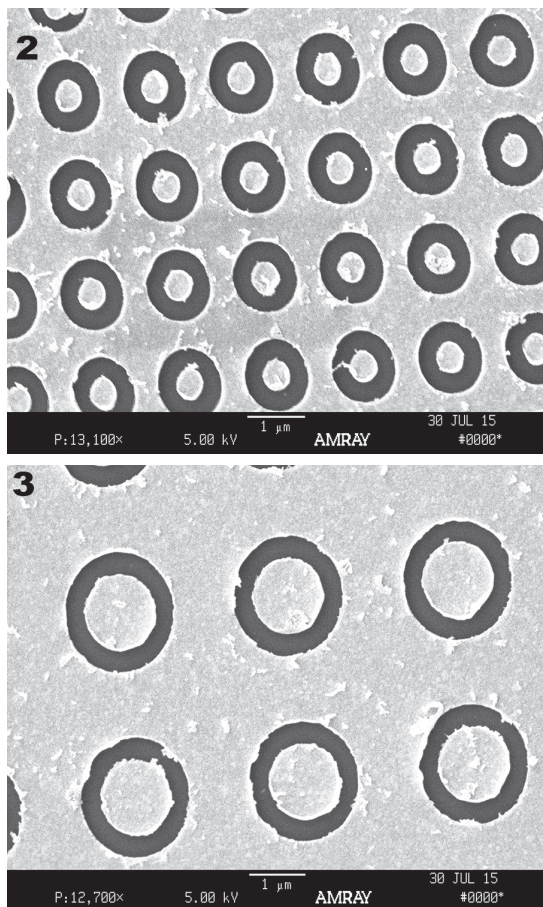


Figure 2, top: 300 nm inner radius annular nanogaps.
Figure 3, bottom: 700 nm inner radius annular nanogaps.

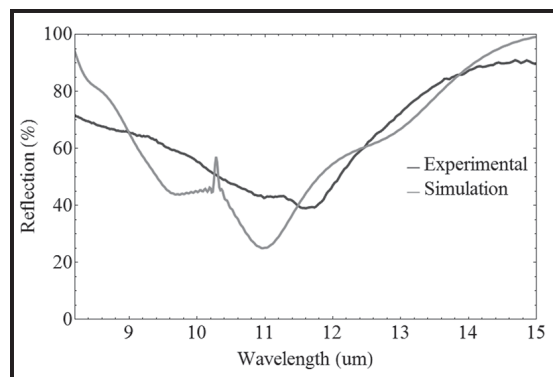


Figure 4: Reflection spectra for 700 nm inner radius sensors.

Results and Conclusions:

We saw some agreement between simulated models and the experimental data, though we did find that there were significant sources of error that contributed to lowering the agreement. One of the sources that we think played the largest part in lowering agreement is erosion of the critical features. This erosion we think came from the wet etching process that was used during the lift off process. The erosion would have occurred unevenly and would have an effect on the resonances. We also noticed that the gold that eroded away often re-deposited on the surface, which may have affected the resonances of the structure. The erosion most likely occurred from the lift-off bath etching the native oxide on the silicon substrate, undercutting the edges of the critical features. The lift-off method use will not etch calcium fluoride to the same degree, so it is unlikely that undercutting will be an issue in the future.

To conclude, annular nanogaps were fabricated for potential applications in plasmonic sensing and spectroscopy. In the future, fabrication of the annular nanogaps on calcium fluoride substrates will be completed. We will then take measurements with the sensors and compare the experimental data with simulated data to determine viability of the sensors as biosensors in real-world applications.

Acknowledgments:

I would like to acknowledge Professor Sang-Hyun Oh and his research group, specifically my mentors Daniel Mohr, Daniel Klemme, and Daehan Yoo, for their assistance in this research. I would like to thank James Marti for his assistance and oversight. I would like to thank the Minnesota Nano Center for use of their facilities. I would also like to thank the National Nanotechnology Infrastructure Network Research Experience for Undergraduates Program for giving me this opportunity to research. This research was supported by the National Science Foundation under Grant No. ECCS-0335765.

Quantum Dot Superlattice Hybrid Structures for Solar Cell Applications

Rachel Lucas

Physics/Aerospace Engineering, Purdue University

NNIN iREU Site: National Institute for Materials Science (NIMS), Tsukuba, Ibaraki, Japan

NNIN iREU Principal Investigators: Dr. Takeshi Noda, High Efficiency Solar Cell Group, NIMS, Tsukuba, Ibaraki, Japan;

Professor Hiroyuki Sakaki, Toyota Technological Institute, Nagoya, Aichi, Japan

NNIN iREU Mentor: Dr. Martin Elborg, High Efficiency Solar Cell Group, NIMS, Tsukuba, Ibaraki, Japan

Contact: lucas27@purdue.edu, noda.takeshi@nims.go.jp, elborg.martin@nims.go.jp

Introduction:

Using quantum structures (Qs) in the absorption layer of a solar cell has been of great interest in potentially overcoming the Shockley-Queisser conversion efficiency limit of solar cells. Qs produce an intermediate band (IB) that allows absorption of sub-bandgap photons and thus increases photocurrent generation [1]. This process occurs in two steps wherein one photon excites a carrier from the valance band (VB) to the IB and a second photon excites this carrier from the IB to the conduction band (CB). This process is called two-step photocurrent generation (Figure 1) and it increases the number of carriers reaching the CB thus increasing the current created.

A hybrid quantum dot (QD) quantum well (QW) structure was proposed as a method to create intermediate energy states. This hybrid structure is expected to provide advantages of both QWs and QDs, surpassing the issues of using only one type of quantum structure. QDs afford a discrete density of states, but large absorption of light requires many layers of QDs, which is difficult to realize. QWs allow a relatively large absorption of photons however two-step photocurrent generation is less efficient when light is incident perpendicular to this structure. Using both structures is expected produce a combination of all desired traits.

A GaAs/AlGaAs superlattice (SL) structure and InAs QDs were grown and intermediate band solar cells (IBSC) were fabricated from them. In this work carrier transfer between the SL and QD structures was studied in addition to two-step photocurrent generation.

Fabrication Procedure:

A superlattice structure of ten 4 nm thick GaAs wells separated by 3 nm thick AlGaAs barriers was grown beneath an InAs QD layer. The QDs were grown using the Stranski-Krastanov growth mode. In this growth mode, the initial growth proceeds layer-by-layer until a critical thickness is reached. A further deposition of the material causes the growth mode to change from two-dimensional to three-dimensional creating dots. This hybrid structure was grown between layers of AlGaAs on a p-type GaAs <100> substrate. All samples were grown using molecular beam epitaxy (MBE). Solar cells were fabricated using photolithography, sputtering, and chemical etching. The devices were then packaged and bonded for testing.

Results:

Atomic force microscopy (AFM) was used to characterize the QDs. Approximate QD density was found to be $6.6 \times 10^{10} \text{ cm}^{-2}$, while approximate dot size was found to be 20 nm in diameter and 2 nm in height. Photoluminescence (PL) measurements performed at 10 K revealed that SL emission energy was 1.6 eV while QDs had a broad curve of emission energies peaking at 1.4 eV (Figure 2).

Through a comparison of the sample containing only the SL structure and the sample containing both SL and QD structures it is seen that the intensity of the SL peak decreases with the addition of QDs to the sample structure. This indicates that carriers are being transferred out of the SL and into the QDs in the hybrid structure.

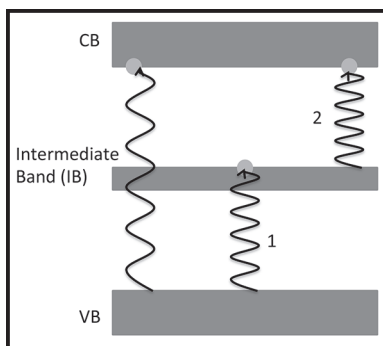


Figure 1: Band diagram of two-step photocurrent generation where 1 marks the transition from VB to IB due to one photon and 2 marks the transition from IB to CB due to a second photon.

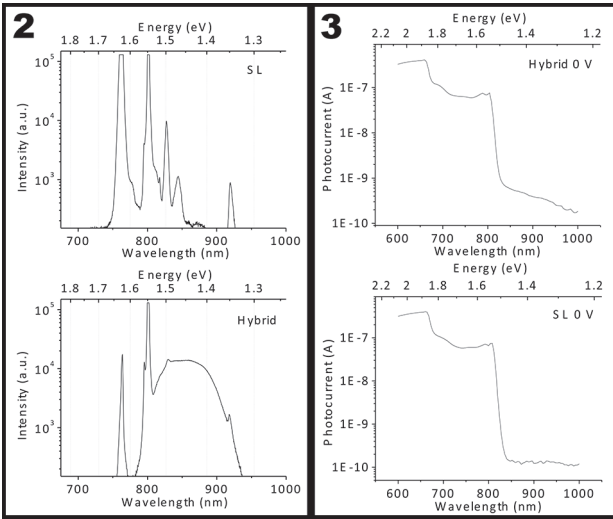


Figure 2, left: Photoluminescence data for superlattice and hybrid samples. Figure 3, right: Photocurrent data for superlattice and hybrid solar cell samples.

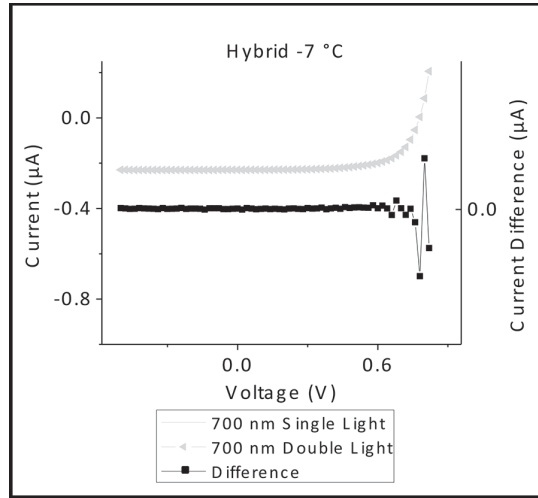


Figure 4: Room temperature two-step photocurrent generation for hybrid sample. Squares correspond to the right-hand y-axis while triangles correspond the left-hand axis.

Photocurrent measurements performed on the solar cell samples at room temperature (RT) reveal a step-like structure for each of the samples (Figure 3). These steps appear because of the sample's dependence of carrier generation on incident light energy. Light having energies greater than 1.9 eV can create carrier pairs throughout the entire solar cell sample. Therefore light with these energies produces the largest photocurrent. Between 1.9 eV and 1.5 eV light no longer has enough energy to create carrier pairs in AlGaAs causing a drop in photocurrent. A second, larger drop in photocurrent occurs at energies below 1.5 eV because carrier pairs can no longer be created in the SL structure. It is seen beyond this second drop in photocurrent that the addition of QDs to the structure causes a small increase in photocurrent by absorbing longer wavelengths.

A 1.55 μm laser was used along with a 700 nm (1.77 eV) monochromatic light source to investigate two-step photocurrent generation. The 700 nm light creates the carrier pairs while the laser is expected to excite these carriers from trapping in QDs to generate additional photocurrent. However, when the samples were lit with the laser there was no visible current difference than when only lit with the 700 nm light (Figure 4). In addition, saturated photocurrent flows until the voltage is close to the open circuit voltage. This indicates that the carriers escape trapping due, presumably, to thermal escape processes without the need for the laser. Therefore no two-step photocurrent generation is seen at RT.

Conclusions and Future Work:

Growth of solar cell structures was successful as indicated by photocurrent spectra and current generation in current-voltage (IV) curves. Carrier transfer was confirmed from the SL to QD structures in PL data. In measurements at RT, however, two-step photocurrent generation was not observed in samples. This is explained by no or negligible carrier trapping at RT due to thermal escape processes. Low temperature measurements or adjusting the SL and QD hybrid structure are future works in order to prove the possibilities of our proposed structure.

Acknowledgements:

Thanks to Dr. Takeshi Noda, Dr. Hiroyuki Sakaki, and Dr. Martin Elborg as well as the High Efficiency Solar Cell/Quantum Nanostructures Group. Thank you to the National Nanotechnology Infrastructure Network International Research Experience for Undergraduates and the NSF, Grant No. ECCS-0335765, for funding and thanks to NIMS.

References:

- [1] Jo, M., Y. Ding, T. Noda, T. Mano, Y. Sakuma, K. Sakoda, L. Han, and H. Sakaki. "Impacts of Ambipolar Carrier Escape on Current-Voltage Characteristics in a Type-I Quantum Well Solar Cell." *Applied Physics Letters* 103,061118 (2013).

Multidimensional Metal-Dielectric Plasmonic Array

Quang Nguyen

Engineering Physics, Case Western Reserve University

NNIN REU Site: Lurie Nanofabrication Facility, University of Michigan, Ann Arbor, MI

NNIN REU Principal Investigators: Dr. Somin E. Lee, Biomedical Engineering, University of Michigan;

Dr. Young Geun Park, Chemical Engineering, University of Michigan

NNIN REU Mentor: Dr. Young Geun Park, Chemical Engineering, University of Michigan

Contact: nguyenq12@gmail.com, slee@umich.edu, ygpark@umich.edu

Abstract:

We present a new multi-dimensional plasmonic array consisting of a metal-dielectric-metal interface. This array enhances plasmonic interactions between layers and exhibits tunneling effects dependent on dielectric thicknesses. Plasmon-driven growth is used to controllably fabricate the multi-layer nanogap structure. This multi-dimensional structure, which cannot be easily produced through conventional lithographic methods, takes advantage of plasmonic coupling effects and provides increased tunability of the optical resonance as well as greater enhancement of the near-field. In addition, we report high electric field focusing in the multidimensional plasmonic nanogap array, which confirms the enhancing nature of the structure and shows a potential for high sensitivity in detection applications. We demonstrate the uniformity and stability of the plasmonic structures through characterization of nanoparticle size and absorption spectra. Such a substrate can find uses in many areas, including optofluidic platforms for the detection of biological molecules such as proteins.

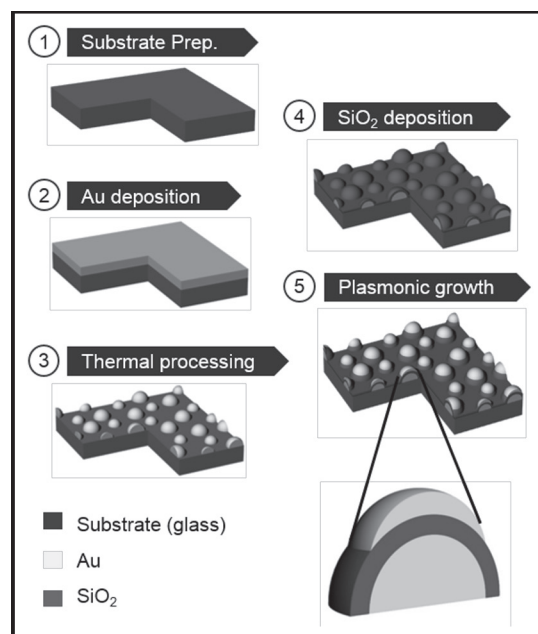


Figure 1: Schematic illustration of fabrication process for the multidimensional array.

Introduction:

In recent years there has been extended exploration of plasmonic substrates due to their uniquely enhanced optical properties that are a result of localized surface plasmon resonances (LSPRs). Such substrates have largely consisted of either isolated or ordered two-dimensional metallic nanostructures in various shapes and sizes. Some examples of shapes that have been prepared include spheres, pyramids, cubes, bowties, rods, stars, and other varied shapes [1].

Much effort has been placed into optimizing geometric properties because the optical characteristics of a plasmonic structure depend critically on features like shape, size, particle spacing, etc. [2]. However, as a result of the focus on shape alteration, relatively little work has been done on increasing the dimensionality of plasmonic structures, which can lead to new interactions and emergent phenomena.

Here we introduce a multi-dimensional plasmonic array that consists of two metal nanostructure arrays separated by an insulating dielectric layer. The increased dimensionality introduces new coupling effects that must be considered, and the solid dielectric layer (as compared to the empty space of air) means that the substrate will exhibit different field decay behavior and see a potential for tunneling and backscattering effects.

Experimental Procedure:

After thoroughly cleaning bare glass slides, gold (Au) films were deposited onto the glass through electron-beam evaporation. The samples were thermally processed by heating in a furnace to produce islands of Au, which comprised the nanogap array of the first layer of nanoparticles (NPs). Then, using SiO₂ as the insulator, the dielectric layer was deposited over the Au NP array through e-beam evaporation.

The second layer of Au NPs was grown on top of the SiO₂ layer through a seed-mediated, plasmon-induced method. We first immersed the samples in an Au seed solution and ensured seed adsorption by taking advantage of the electric field produced by LSPR excitations, which attracted the seeds to adhere to the surface of the previously produced NPs. Then, we grew the second layer of Au NPs on the seeds by chemical reduction of an Au precursor, attracting the Au ions in the same manner using LSPR excitations. In this way, we could direct the growth sites of the secondary Au layer.

Results and Conclusions:

We proceeded to analyze the morphological and optical properties of our plasmonic array to produce a rigorous characterization. To confirm the structure of the substrate we used scanning electron microscopy (SEM) in combination with an image analysis program, ImageJ, to visually as well as quantitatively describe the geometry of the NPs.

From Figure 2, it is evident through simple visual inspection that the number of Au NPs grown in the second metal layer, shown by the white spheres, increased from the controlled growth case to the plasmon-induced growth case. By further analysis in ImageJ, we obtained size distribution data for the particles as shown in Figure 3. The effect of introducing our plasmon-induced method to the growth process was that the size of the NPs grown

with the method was increased at all SiO₂ thicknesses over the control growth.

We demonstrate that the overall size of the NPs, as well as the size difference between the control and experimental cases, decreases with increasing SiO₂ thickness. This result is expected as with a larger insulating layer, the strength of the electric field is reduced and the size of the particles grown should be smaller. With a 20 nm SiO₂ thickness, the difference between the plasmon-induced growth method and the control is almost entirely eliminated. We also see that the dielectric layer cannot be eliminated entirely, as that then results in the smallest size of NPs.

Next we characterized our substrate optically through ultraviolet-visible (UV-VIS) spectroscopy. The absorption spectra, shown in Figure 4, demonstrate a redshift of the resonance peaks with increasing silica thickness. The effect of growing the secondary Au layer, in comparison, is a blueshift of the peaks. In the dark or control growth, which produced smaller NPs than the plasmon-induced method, the blueshift is smaller than in the plasmon-induced growth, which produces larger NPs and exhibits a larger blueshift as a result.

Future Work:

Given the complete characterization of our array and its favorable properties as a plasmonic substrate, we will look to integrate it into practical devices that require the sensitivity and robustness of our substrate. Creation of an optofluidic device to allow detection of biological proteins is an application that has many practical uses, and is one in which our bioplasmonics group at the University of Michigan has experience.

Acknowledgments:

This work was performed in part at the Lurie Nanofabrication Facility at the University of Michigan. We would like to acknowledge support from the NNIN REU Program and the NSF under Grant No. ECCS-0335765.

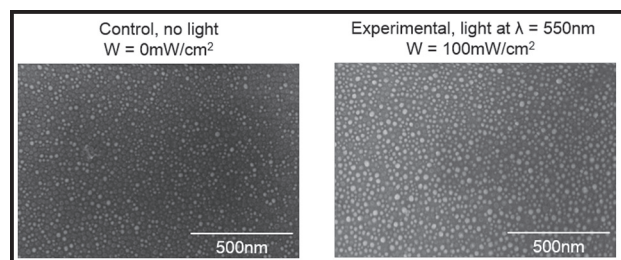


Figure 2: Growth of secondary Au layer without an excitation source (left) and with an excitation source (right).

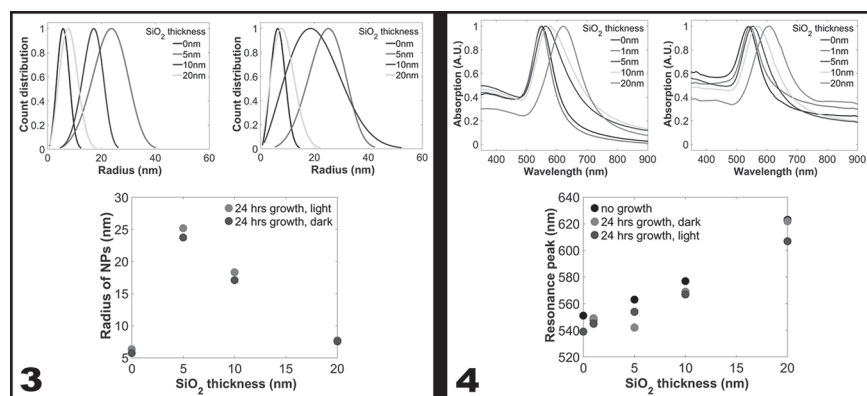


Figure 3, left: Radii of NPs grown without an excitation source (top left), with an excitation source (top right), and comparison of peak location (bottom). Figure 4, right: Absorption spectrum before growth (top left), after 24 hours growth with excitation source (top right), and comparison of peak location (bottom).

References:

- [1] Sharma, Bhavya, et. al. High-performance SERS substrates: Advances and challenges. MRS Bulletin, 2013, 38, 615-624.
- [2] Willets, Katharine A., and Van Duyne, Richard P. Localized Surface Plasmon Spectroscopy and Sensing. Annual Review of Physical Chemistry, 2007, 108, 267-297.

Magnetic Fano Interferences in Plasmonic Metal Oligomers

Claire West

Physics, University of California, Santa Barbara

NNIN REU Site: Washington Nanofabrication Facility and Molecular Analysis Facility, University of Washington, Seattle, WA

NNIN REU Principal Investigator: Professor David Masiello, Chemistry, University of Washington

NNIN REU Mentors: Dr. Charles Cherqui and Steven Quillin, Chemistry, University of Washington

Contact: clairewest@uic.ucsb.edu, masiello@chem.washington.edu, cherqui@uw.edu quills@uw.edu

Abstract:

Plasmonic metal nanoparticles possess exotic optical properties impacting a variety of fields from basic science to energy, defense, and medicine. One such property of broad importance is a Fano interference. This interference can be modeled by two coupled charged oscillators, in which the driven bright mode transfers its energy to the dark mode and stops. Thus, the system is still absorbing energy, but does not scatter. The resulting localization of energy is dependent on the coupling strength and mass ratio of the oscillators. These parameters, when properly tuned, alter the Lorentzian nature of the scattering spectrum, leading to an asymmetric Fano lineshape. The conditions that produce a Fano lineshape in the oscillator model were used to predict parameters in electric and magnetic plasmonic nanoparticle systems. This research focused on showing magnetic-magnetic Fano interferences for the first time. In particular, a magnetic plasmon was created from a cyclic assembly of metal nanospheres each with an electric dipole oriented head-to-tail around the ring, mimicking an electrical current loop. A second plasmonic ring was coupled to the first and driven by an electron beam, and their resulting interference was studied through numerical simulations of Maxwell's equations.

Introduction:

Plasmonic nanoparticle assemblies offer a variety of tunable properties that are highly dependent on the separation of the particles. If the particles are close enough such that the plasmons interfere with each other through near-field interactions, they may experience a Fano interference. This interference is observed by analyzing the light scattered and absorbed from the system, and pinpointing the energy that corresponds to a dip in the scattering spectrum where there is non-zero absorption. This effect has been observed between electric-electric plasmon interferences [1], and electric-magnetic plasmon interferences [2]. But for the first time, this project focused on understanding the Fano interferences between magnetic-magnetic plasmons on a different configurations of nanospheres.

Methods:

The interferences between plasmons were modeled using a damped oscillator system, because the time-dependent dipole moment of a nanosphere in an oscillating electric field is proportional to the Green's function of the damped harmonic oscillator. Figure 1 shows a schematic of this model. The Hamiltonian of this system can be diagonalized to solve for the new hybridized eigenmodes, which represent the electric dipole orientations. The parameters of this model were tuned until the Fano lineshape was most clearly seen in the spectra, which occurred when the masses of the oscillators were different and when the coupling was small. For the first time, this understanding of which parameters produced Fano interferences was used in an attempt to induce a Fano interference between two magnetic modes.

A nanosphere configuration motivated by previous research [3] was adapted to excite a magnetic plasmon Fano interference. Cherqui, et al., excited a ferromagnetic and antiferromagnetic mode on a hexamer oligomer configuration as shown in Figure 2a. An electron-beam was placed next to one sphere to excite the electric dipole on that sphere to point in a given direction and polarize the other dipoles.

The two eigenmodes under consideration were the modes that corresponded to the dipoles orienting head-to-tail because they produced a ferromagnetic and an

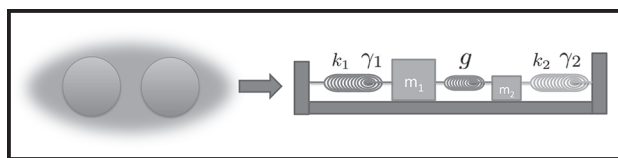


Figure 1: Oscillator system to model plasmonic interferences where k_1 , k_2 , and g represent spring constants, and γ_1 and γ_2 represent damping coefficients.

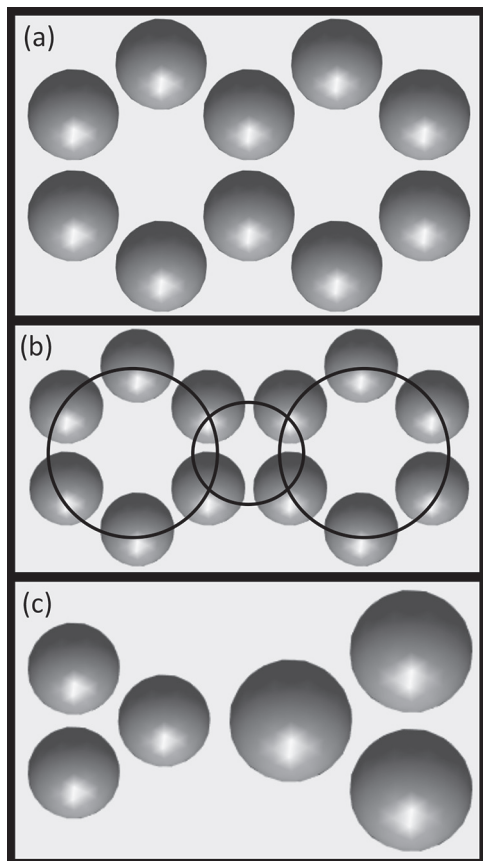


Figure 2: (a) Fused ring system motivated by Cherqui, et al. (b) Separated hexamer system with three magnetic moments circled. (c) New triangular configuration to eliminate third magnetic moment.

antiferromagnetic mode. As learned from optimizing the parameters in the oscillator model, the coupling between the modes had to be small, and therefore the hexamer oligomer configuration was modified by separating the hexamers.

Results and Conclusions:

Ferromagnetic and antiferromagnetic modes created from plasmonic nanoparticle systems were attempted to be excited through numerical simulations on two different nanosphere arrangements. The separation of the rings and the placement of the electron beam were independently varied to excite the two different modes.

In the two hexamer system, the ferromagnetic mode could not be excited due to interferences generated from a magnetic moment that formed from a third electric dipole loop, shown in Figure 2b. Therefore, a new configuration was considered with two separated triangular nanosphere assemblies as shown in Figure 2c. Through various placements of the electron beam and separation distances of the triangular rings, it was realized that although this configuration corrected the previous problem, the

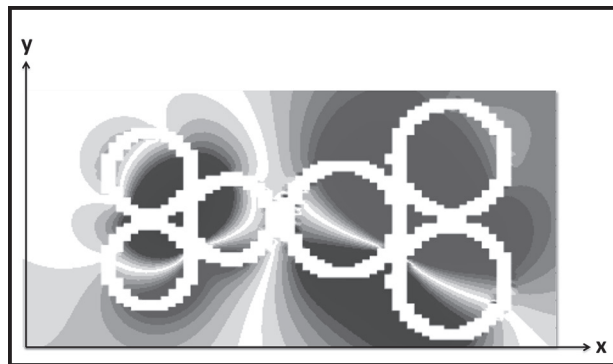


Figure 3: Magnetic fields in triangular system did not form localized moments.

magnetic modes did not completely close in and become localized, as shown in Figure 3.

In conclusion, by changing the ring separation and electron beam placement in two different configurations, a ferromagnetic mode was never excited.

Future Work:

For the future work on this project, a new configuration must be considered in order to excite these two localized magnetic modes. One possible system would be to amend the triangular arrangement and add a fourth nanosphere to each triangle in order to form the magnetic modes.

Once this system achieves the desired ferromagnetic and antiferromagnetic modes, the scattering spectra can be analyzed to find the Fano interference. The ring distance and nanosphere separation can be varied and optimized to analyze which conditions produce the Fano effect.

Acknowledgments:

This work was supported by the National Science Foundation's NNIN Research Experience for Undergraduates Program via grant number ECCS-0335765. I would like to thank Professor David Masiello for supervising me, and Charles Cherqui, Steven Quillin, Nick Montoni, and Niket Thakket for advising me during this project. I would also like to thank Melanie-Claire Mallison for organizing this program.

References:

- [1] Lovera, A.; Gallinet, B.; Norlander, P.; Martin, O. Mechanisms of Fano Resonances in Coupled Plasmonic Systems. *ACS Nano* 2013, 7, 4527-4536.
- [2] Sheikholeslami, S. N.; Garca-Etxarri, A.; Dionne, J. A. Controlling the Interplay of Electric and Magnetic Modes via Fano-like Plasmon Resonances. *Nano Letters* 2011, 11, 3927-3934.
- [3] Cherqui, C.; Bigelow, N.; Vaschillo, A.; Goldwyn, H.; Masiello, D. Combined Tight-Binding and Numerical Electrodynamics Understanding of STEM/EELS Magneto-optical Responses of Aromatic Plasmon-Supporting Metal Oligomers. *ACS Photonics* 2014, 1, 1013-1024.